

TOWARD GRAVITATIONAL WAVEFORMS FOR EXTREME AND INTERMEDIATE  
MASS RATIO INSPIRALS OF BLACK HOLE BINARY SYSTEMS: STRATEGIES  
FOR COMPUTING THE SELF-FORCE OF A SCALAR FIELD ON A  
SCHWARZSCHILD SPACETIME BACKGROUND DUE TO CAUSAL  
CONNECTIONS BETWEEN THE PARTICLE'S PAST ORBIT AND PRESENT  
POSITION USING THE DISCONTINUOUS GALERKIN, EFFECTIVE SOURCE,  
AND OSCULATING ORBIT METHODS

A Thesis/Dissertation

Submitted to the Graduate Faculty of the  
Louisiana State University and  
Agricultural and Mechanical College  
in partial fulfillment of the  
requirements for the degree of  
Master of Science

in

Physics

by

Steven (Susan) Dorsher

B.S., Massachusetts Institute of Technology, 2004

M.S., The Ohio State University, 2006

M.S., University of Minnesota, 2013

December, 2017

# Acknowledgments

I would like to thank Peter Diener and Frank Löffler for their guidance. Peter Diener especially has been very important to me, both as an advisor and personally. I would also like to thank Gabriela Gonzalez for the excellent opportunity to work on LIGO during the time of three detections, which provided me the funding I needed to continue the work detailed in this document. I would like to thank Juana Moreno for the opportunity to work as outreach coordinator to the LA-SIGMA Research Experience for Undergraduates program my first summer at LSU, which also helped provide funding for this research. My parents, Paul and Joanne Dorsher, also deserve a mention, both for extraordinary moral support and for the financial support they provided that helped make this possible. I would also like to thank my sister, Patricia Dorsher.

# Table of Contents

ACKNOWLEDGMENTS .....	ii
LIST OF TABLES .....	iv
LIST OF FIGURES .....	v
ABSTRACT .....	vii
CHAPTER	
1 INTRODUCTION .....	1
1.1 Gravitational Waves .....	1
1.2 Extreme Mass Ratio Inspirals .....	4
1.3 EMRIs .....	4
1.4 The discontinuous galerkin method .....	4
1.5 LISA .....	4
2 A SIMPLE NUMERICAL SOLUTION FOR A PDE USING THE DISCONTINUOUS GALERKIN METHOD .....	5
2.1 The Discontinuous Galerkin method .....	5
2.2 Separation of variables .....	5
2.3 Wave equation on flat spacetime .....	5
3 A SCALAR FIELD ON A SCHWARZSCHILD BACKGROUND WITHOUT A SOURCE .....	8
3.1 Scalar field on Schwarzschild spacetime .....	8
3.1.1 Multipole moment decomposition .....	8
3.1.2 Hyperboloidal compactification .....	8
3.1.3 Initial conditions .....	8
3.1.4 final results .....	8
4 CIRCULAR ORBITS ON A SCHWARZSCHILD SPACETIME .....	13
4.1 $\phi$ of $t$ .....	13
4.1.1 Effective source .....	13
4.1.2 World tube .....	13
4.1.3 Comparison between C++ and Fortran codes .....	13
5 ELLIPTICAL ORBITS ON A SCHWARZSCHILD SPACETIME .....	17
5.0.1 Time dependent coordinate transformation .....	17
5.0.2 orbital parameters (osculating orbits paper) .....	17
5.0.3 precession figure .....	17
6 EXTRAPOLATING THE SELF FORCE TO INFINITE DISCONTINUOUS GALERKIN ORDER .....	19

6.0.1	Checking for discontinuities in $F_{\text{inf}}$ for each each l-mode .....	19
6.0.2	Determining $F_{\text{inf}}$ using maximum likelihood fits to subsegments of lines in semilog space .....	21
7	EXTRAPOLATING THE MODE-SUMMED SELF-FORCE TO INCLUDE CONTRIBUTIONS FROM AN INFINITE NUMBER OF SPHERICAL HARMONIC MODES.....	28
7.0.1	Relative error as a function of mode .....	28
7.0.2	Fractional errors.....	31
7.0.3	Structure of the error compared to the evolu- tion in time .....	31
8	FUTURE WORK: GENERIC ORBITS VIA THE OSCU- LATING ORBITS FRAMEWORK.....	35
8.1	plans for the future .....	35
8.1.1	methods .....	35
	REFERENCES.....	36
	VITA .....	38

# List of Tables

6.1	Manual starting indices and $F_{\text{inf}}$ values for $t=632$ , $l=2$ . . . . .	19
-----	---	----

# List of Figures

2.1	Waves evolving over time for gaussian initial conditions .....	6
2.2	Waves evolving over time for sinusoidal initial conditions .....	6
2.3	$L_2$ error scaling with DG order for sinusoidal initial conditions .....	7
2.4	$L_2$ error scaling with element size for sinusoidal initial conditions .....	7
3.1	Quasinormal mode for $l=1, m=1$ .....	9
3.2	Quasinormal mode for $l=2, m=2$ .....	9
3.3	Power law tail, $l=1, m=1$ .....	10
3.4	Power law tail does not match expectations due to truncation error in DG method, $l=2, m=2$ .....	10
3.5	Scalar field spatial slice initial condition and first full timestep for $l=0$ . .....	11
3.6	Time derivative of the scalar field spatial slice initial condition and first full timestep for $l=0$ . .....	11
3.7	Radial derivative of the scalar field spatial slice initial condition and first full timestep for $l=0$ . .....	12
4.1	Spatial slice of the world tube window function. ....	14
4.2	Add or subtract the singular field to either side of the world tube boundary before performing the time dependent coordinate transform (or inverting it) to obtain the retarded field in the exterior region and the regularized field in the interior region. ....	14
4.3	Comparison between Fortran and C++ codes for a particle on a circular orbit, $l=0, m=0$ . ....	15
4.4	Comparison between Fortran and C++ codes for a particle on a circular orbit, $l=1, m=1$ . ....	15
4.5	Comparison between Fortran and C++ codes for a particle on a circular orbit, $l=2, m=0$ . ....	16
4.6	Comparison between Fortran and C++ codes for a particle on a circular orbit, $l=2, m=2$ . ....	16

5.1	470 M near perihelion, 640 M at aphelion .....	18
6.1	DG convergence with order, extrapolated from highlighted points to infinite order along exponential form, which appears as a straight line in the semilog plot. ....	20
6.2	Starting order was chosen by iterating from the lowest order to the first order for which the “mode failed”, and choosing the maximum starting order that succeeded. When $F_{\text{inf}}$ is evolved over one full orbital cycle, some l-modes shows discontinuities at some times. $l=3$ .....	21
6.3	Fluctuation in one of the points chosen in the extrapolation, due to roundoff or truncation error, causes the extrapolation to predict a value of $F_{\text{inf}}$ that is subtly wrong, leading to curvature in the semilog plot after $F_{\text{inf}}$ subtraction. $t=632, l=2, i=1$ .....	22
6.4	Roundoff error is visible at high DG orders. $t=632, l=2, i=2$ .....	23
6.5	The incorrect value of $F_{\text{inf}}$ has been chosen due to roundoff error, perhaps due to finite precision in the root finding algorithm, leading to a negative values, that show as a “V” in the semilog plot. $t=632, l=3, i=3$ .....	24
6.6	Manual correction for the discontinuities in the $l=2$ mode, using the manually determined $F_{\text{inf}}$ data from Table ?? .....	25
6.7	An example of no discontinuities in $F_{\text{inf}}$ for any of the l-modes. Mode $l = 0$ . ....	26
6.8	$l=0$ mode with line-segment fit-chosen starting order produces convergence plot with long exponentially converging region .....	27
7.1	Relative error between fit and median techniques increases with l-mode .....	29
7.2	Absolute error between fit and median techniques increases with l-mode .....	29

7.3	This is the relative difference between the total radial self force measured in two different ways. In both cases, the self force was extrapolated to infinite order at every l-mode at every possible DG starting order. The infinite DG order self forces over the various starting orders were sorted, eliminating NaNs. The median was chosen for each l-mode. Then the self force as a function of l-mode was fit to its three term form, and the sum was summed from zero to lmax, then extrapolated from $l_{max} + 1$ to infinity using an analytic form determined using Mathematica. All possible choices with lmin between 14 and 17 and lmax between 22 and 25 were averaged to obtain the total radial self force as a function of time. Similarly, all possible choices with lmin between 14 and 19 and lmax between 24 and 30 were averaged to obtain the total radial self force as a function of time. This plot shows the relative difference. I believe the smaller range is in the denominator. ....	30
7.4	This figure was produced in the same manner as the previous figure, averaging over the smaller range, only it is a comparison between including either two or three terms in the l-mode fit. I believe the three term fit is in the denominator of the relative difference.....	31
7.5	This figure was produced in a similar manner to the first figure, only instead of using the median, it is a comparison between using the median, the maximum, and the minimum. The purple line is the relative difference between the maximum and the median, which is subject to roundoff error due to the potential for the maximum to contain roundoff error. The green line is the relative difference between the median and the minimum, which is subject to effects due to failure to converge. I suspect the median is the best compromise between these two effects, rejecting outliers in both directions, though it is a simplistic approach to doing so, and does not guarantee success. It is possible to have a starting order that has not converged and is also in the roundoff regime, for example. A better guarantee of success, though not a certain one, would be to do a fit over part of the error convergence plot to determine exponentiality, by fitting a line in semilog scale. However, this seems unnecessarily complex at this time. ....	32
7.6	This is the actual summed, doubly extrapolated, radial self force, measured in three different ways as described in the three figures above. ....	33
7.7	3 term, median method.....	33



7.8	3 term, fit method.....	34
7.9	The structure of the absolute error in comparison to the evolution in time for the fit method .....	34

# Abstract

Insert the text of your abstract here. Make sure there is one blank line between the end of the Abstract text and the “end” command below to maintain double-spaced lines.

# Chapter 1

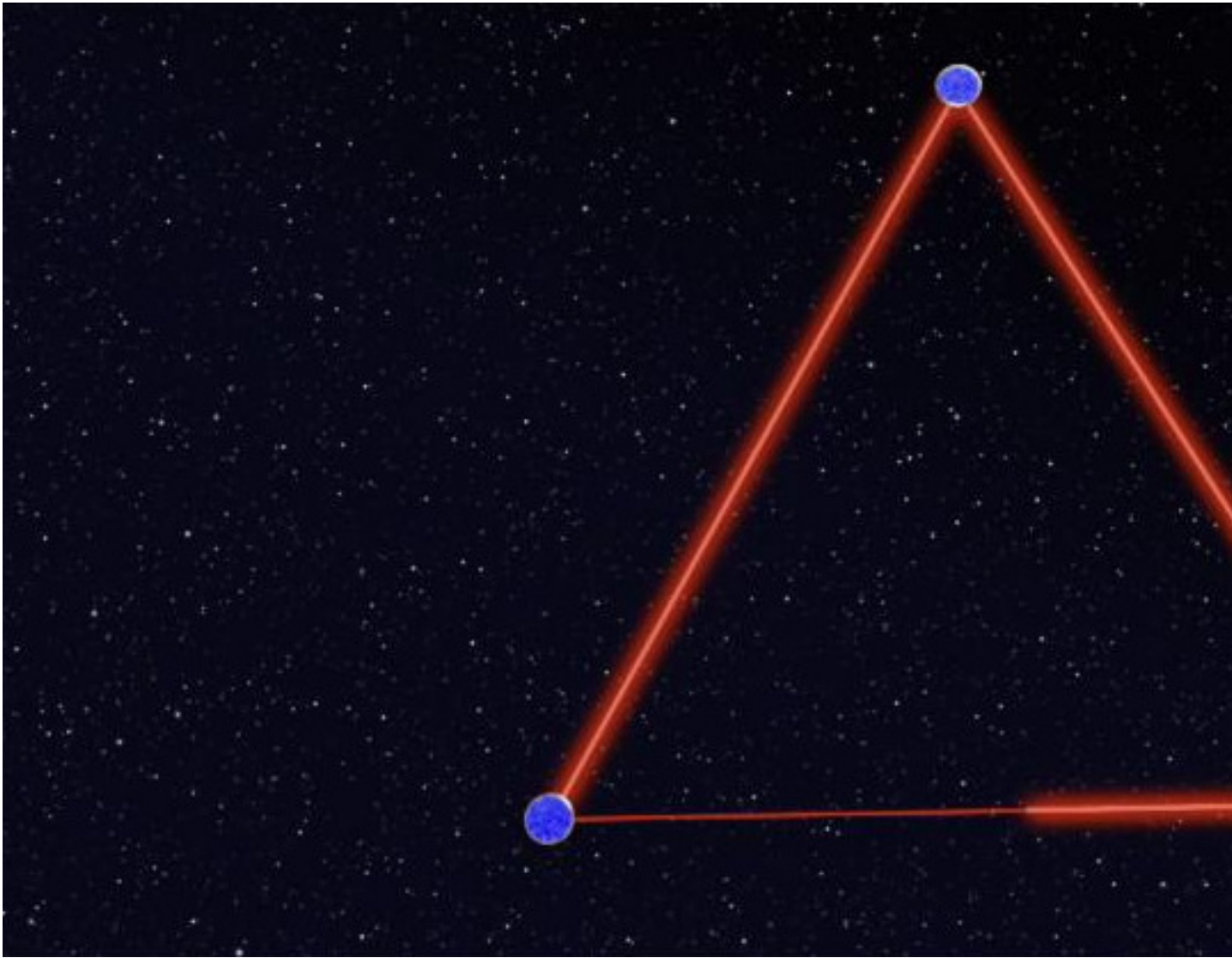
## Introduction

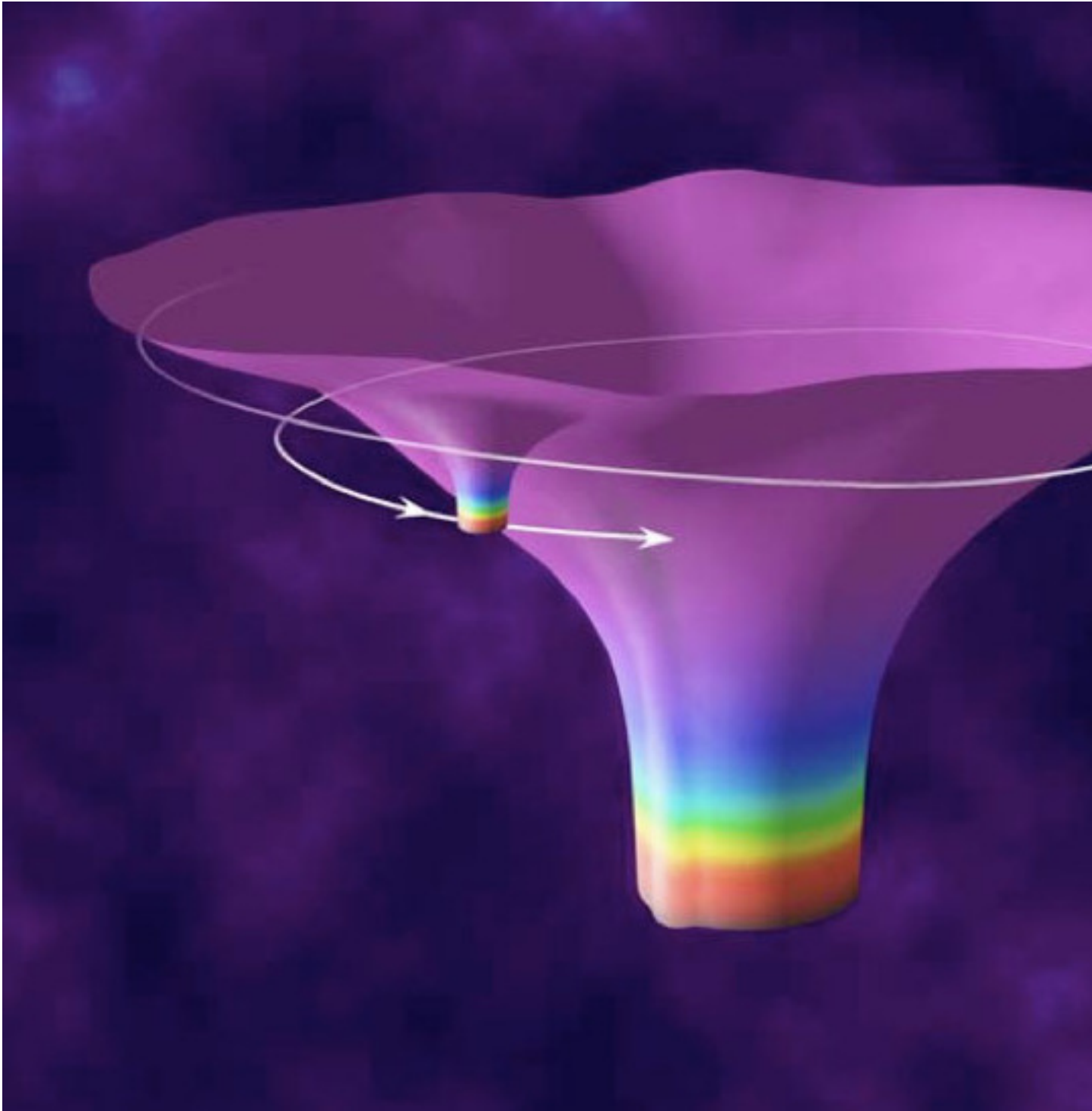
### 1.1 Gravitational Waves

On February 11, 2016, the LIGO Scientific Collaboration announced the first detection of gravitational waves from a black hole binary inspirals, occurring on September 14, 2015, with pre-merger masses of  $36 M_{\odot}$  and  $29 M_{\odot}$  and a post merger mass of  $62 M_{\odot}$  at a redshift of  $z = 0.09$  [1]. Two subsequent detections followed, on December 26, 2015 [2] and on January 4, 2017 [3], with masses that are about the same to within an order of magnitude.

There is a question of what is meant, observationally, by a black hole. Does it need to have a horizon? Does it need to have a Kerr metric (the simplest possible space-time for a spinning black hole in general relativity)? Does it simply need to be a sufficiently compact object that it can't be ordinary nuclear matter? Historically, black holes have been defined by their compactness [15]; however, some studies are beginning to consider tests of horizons [] or of the Kerr metric itself [15]. X-ray binaries, gravitational wave constraints from binary-pulsar systems, active galactic nuclei models containing super-massive black holes on the order of  $10^6 M_{\odot}$ , and the three LIGO detections, as well as black hole formation models, suggest that black holes of all scales should be spinning [15]. However, for the purposes of this manuscript, I will consider non-spinning, spherically symmetric black holes in general relativity, described by the Schwarzschild metric.

Currently, there are four distinct windows on the gravitational wave universe planned or in progress. The Laser Interferometer Gravitational Wave Observatory, LIGO, probably deserves first listing, due to their recent success. LIGO observes gravitational waves using a ground based Michelson-Morley interferometer with two 4 kilometer long Fabry-Perot cavity arms. It detects strains as small as  $10^{-23} Hz^{-1/2}$  [16].





- 1.2 Extreme Mass Ratio Inspirals
- 1.3 EMRIs
- 1.4 The discontinuous galerkin method
- 1.5 LISA

## Chapter 2

# A simple numerical solution for a PDE using the Discontinuous Galerkin method

2.1 The Discontinuous Galerkin method

2.2 Separation of variables

2.3 Wave equation on flat spacetime

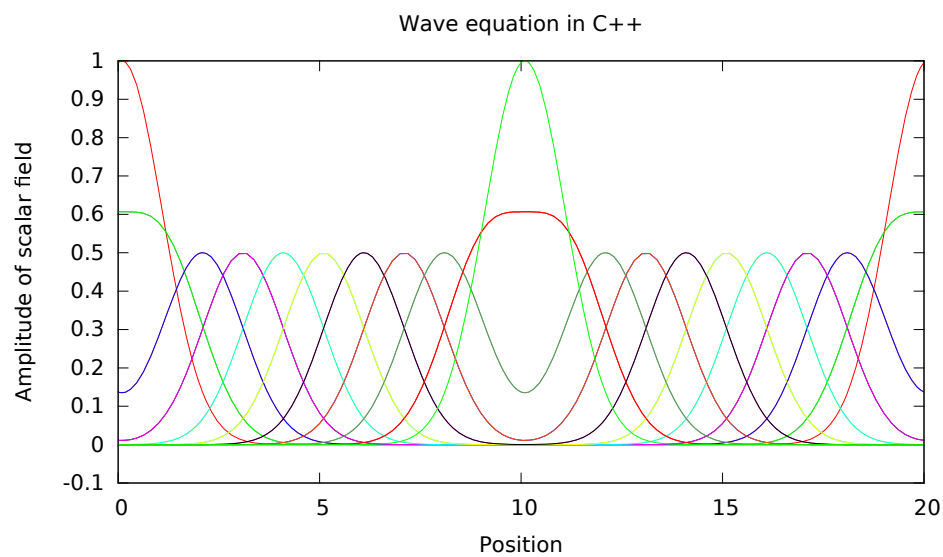


Figure 2.1: Waves evolving over time for gaussian initial conditions

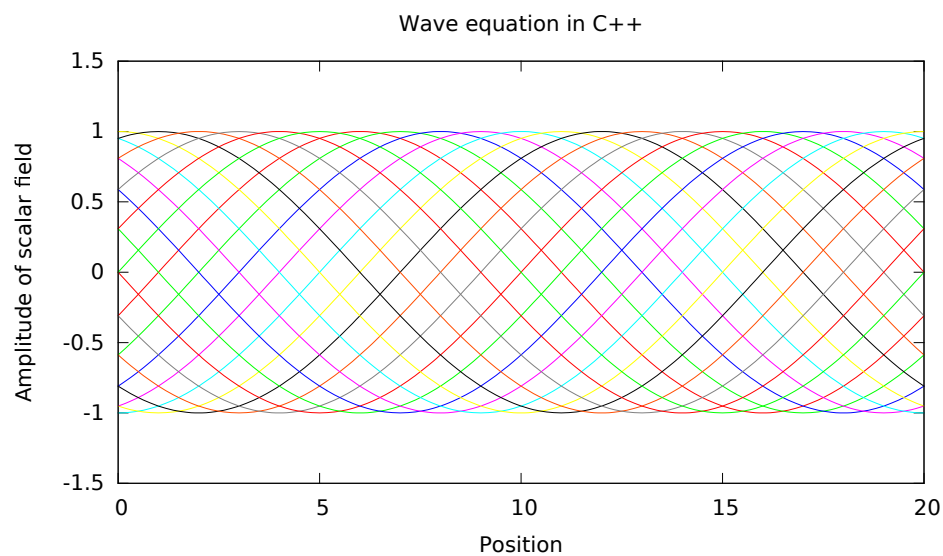


Figure 2.2: Waves evolving over time for sinusoidal initial conditions



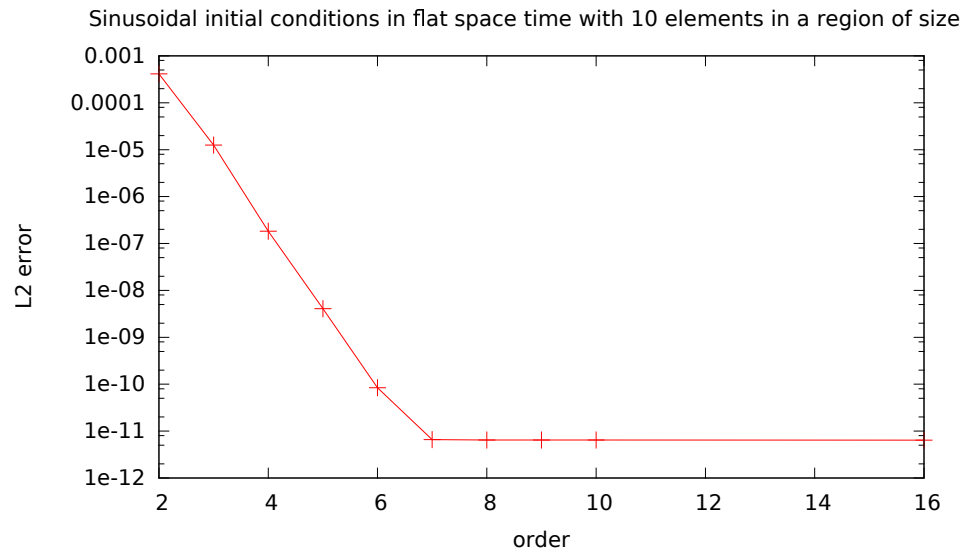


Figure 2.3:  $L_2$  error scaling with DG order for sinusoidal initial conditions

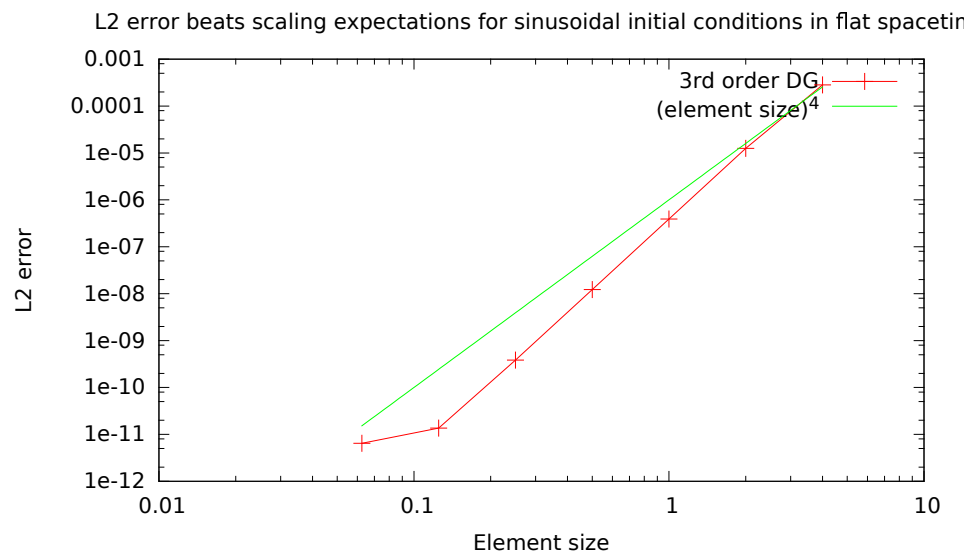


Figure 2.4:  $L_2$  error scaling with element size for sinusoidal initial conditions

# Chapter 3

## A scalar field on a Schwarzschild background without a source

### 3.1 Scalar field on Schwarzschild spacetime

#### 3.1.1 Multipole moment decomposition

#### 3.1.2 Hyperboloidal compactification

Tortoise coordinates and wave equation Wave equation in this form Boundary conditions

#### 3.1.3 Initial conditions

#### 3.1.4 final results

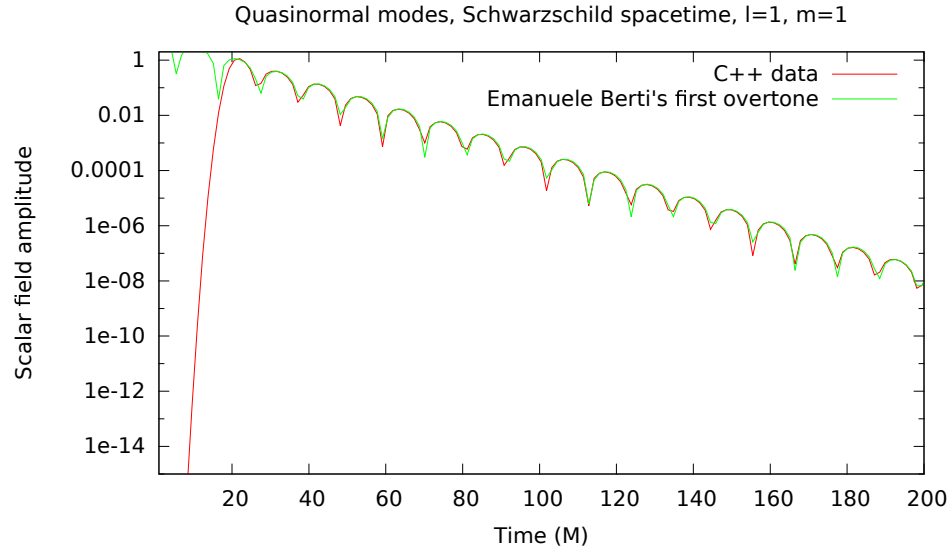


Figure 3.1: Quasinormal mode for  $l=1, m=1$

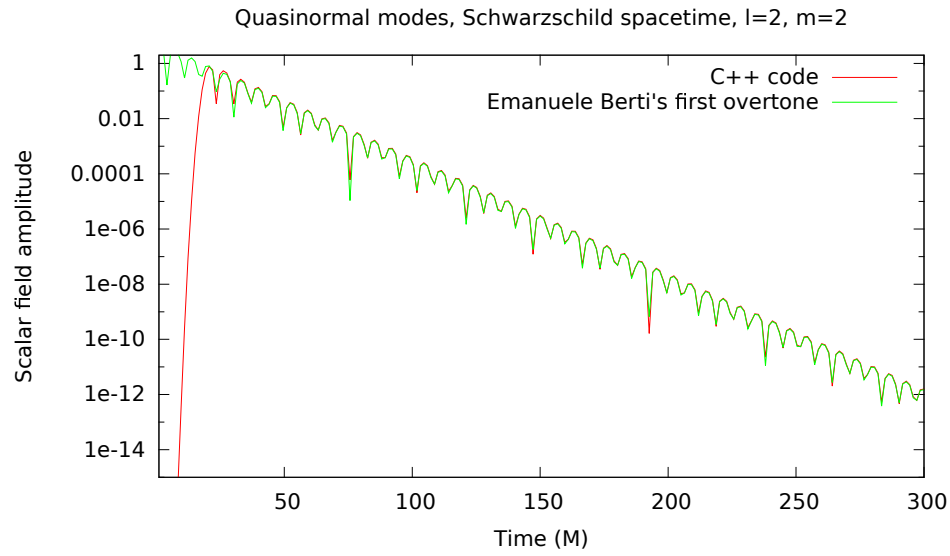


Figure 3.2: Quasinormal mode for  $l=2, m=2$

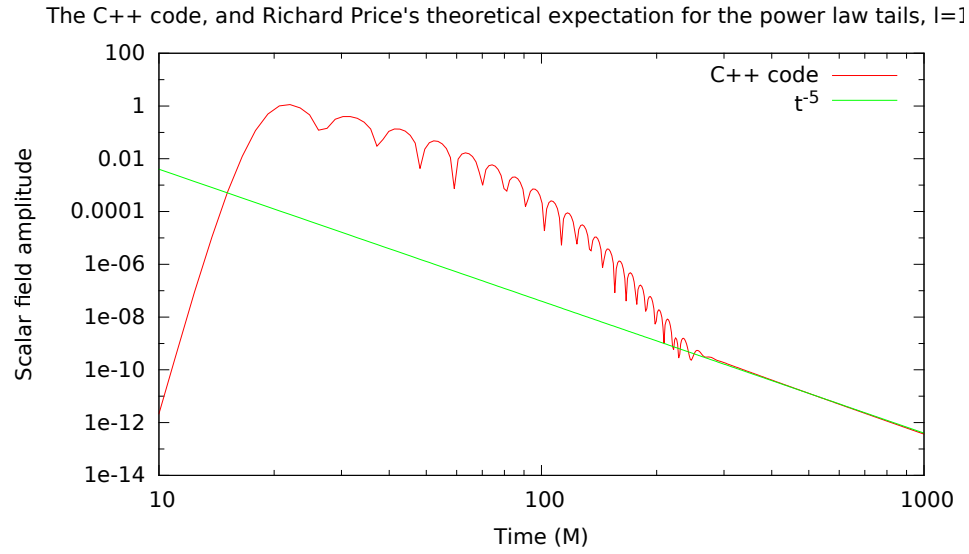


Figure 3.3: Power law tail,  $l=1$ ,  $m=1$

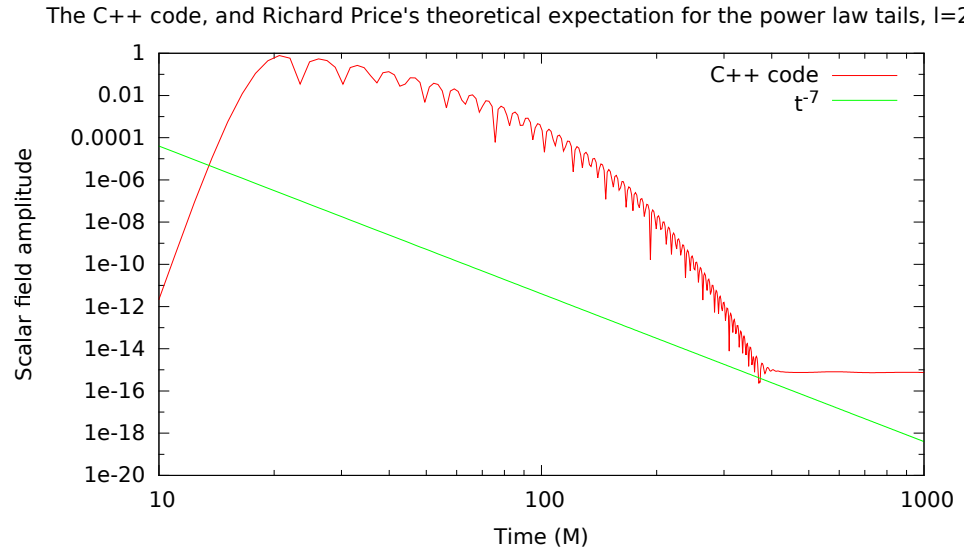


Figure 3.4: Power law tail does not match expectations due to truncation error in DG method,  $l=2$ ,  $m=2$

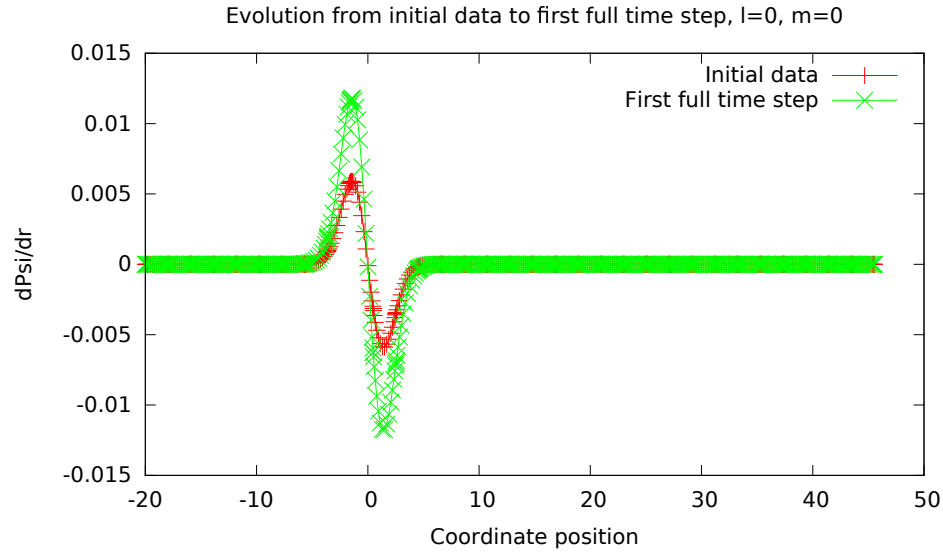


Figure 3.5: Scalar field spatial slice initial condition and first full timestep for  $l=0$ .

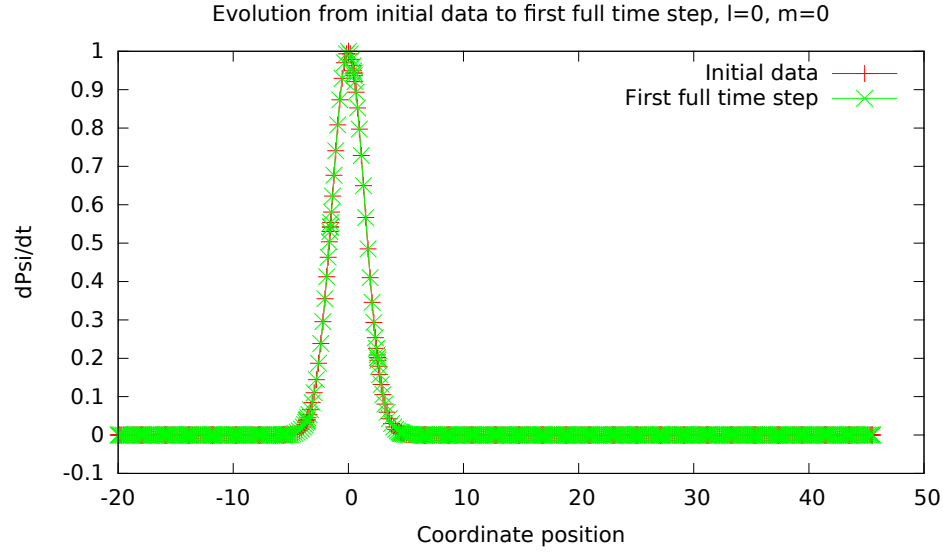


Figure 3.6: Time derivative of the scalar field spatial slice initial condition and first full timestep for  $l=0$ .

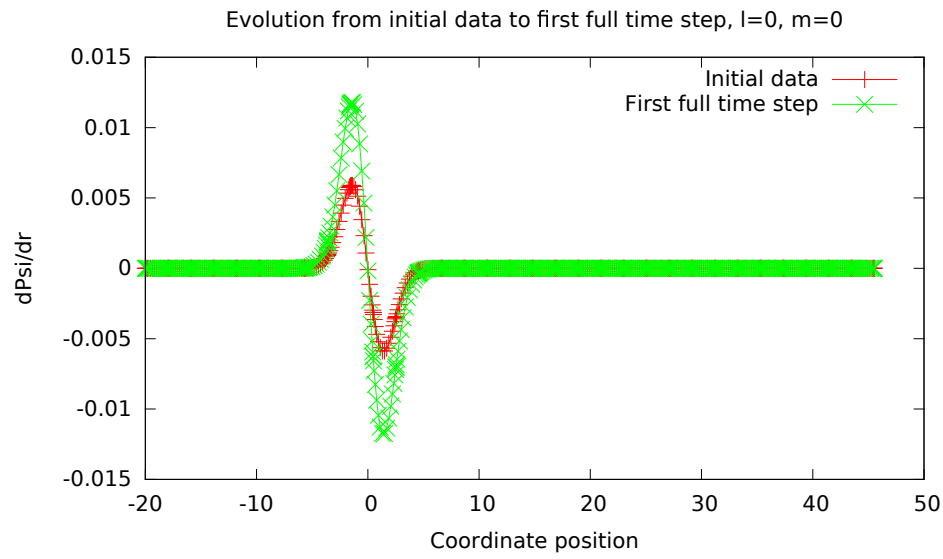


Figure 3.7: Radial derivative of the scalar field spatial slice initial condition and first full timestep for  $l=0$ .

# Chapter 4

## Circular orbits on a Schwarzschild spacetime

### 4.1 $\phi$ of $t$

#### 4.1.1 Effective source

#### 4.1.2 World tube

#### 4.1.3 Comparison between C++ and Fortran codes

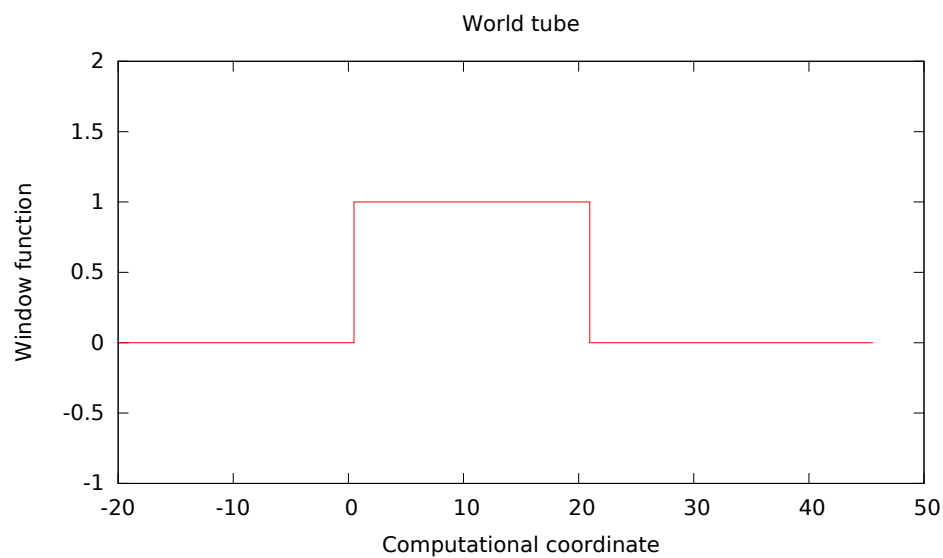


Figure 4.1: Spatial slice of the world tube window function.

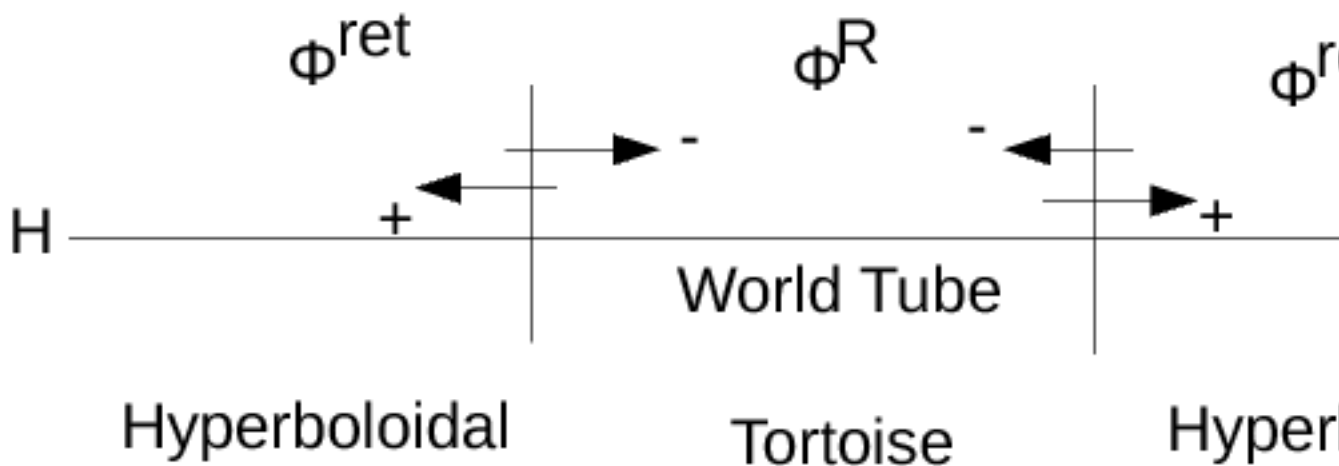


Figure 4.2: Add or subtract the singular field to either side of the world tube boundary before performing the time dependent coordinate transform (or inverting it) to obtain the retarded field in the exterior region and the regularized field in the interior region.



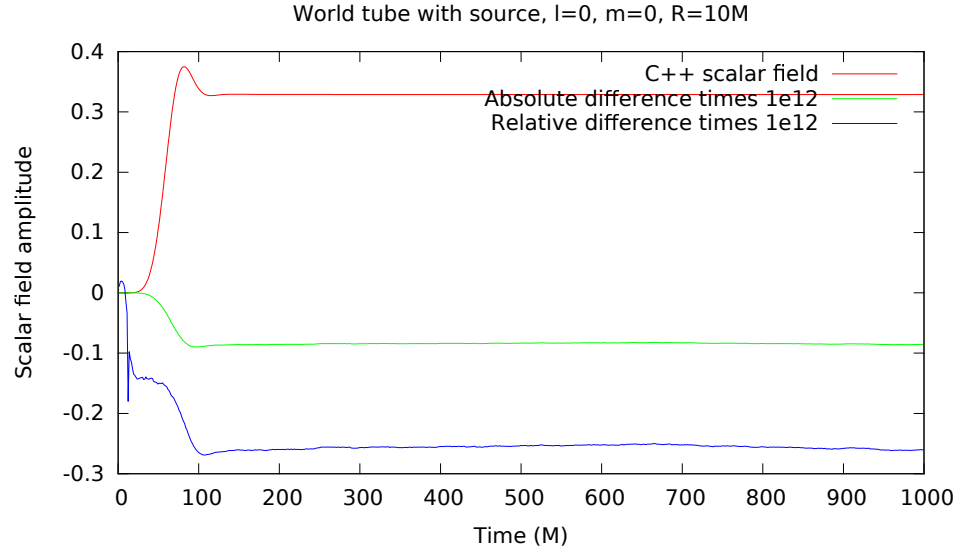


Figure 4.3: Comparison between Fortran and C++ codes for a particle on a circular orbit,  $l=0$ ,  $m=0$ .

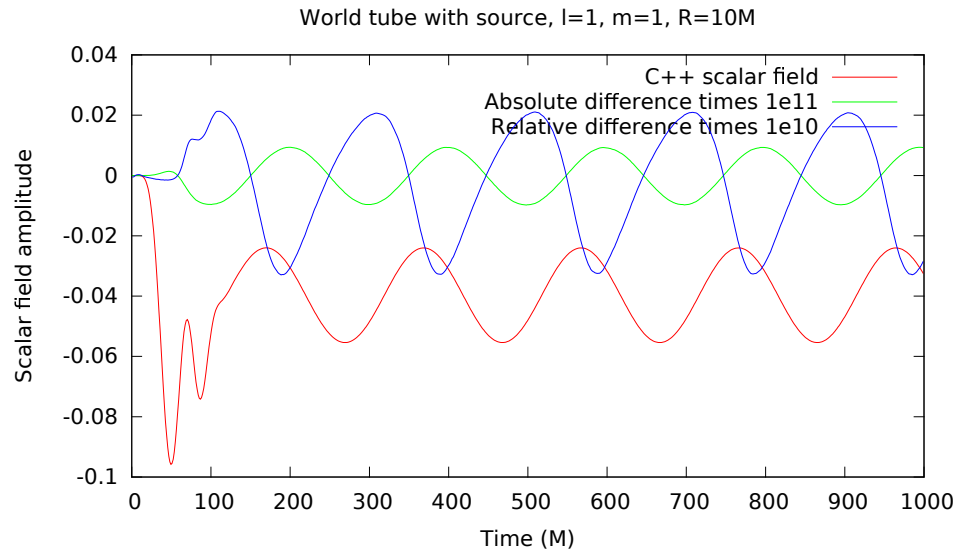


Figure 4.4: Comparison between Fortran and C++ codes for a particle on a circular orbit,  $l=1$ ,  $m=1$ .

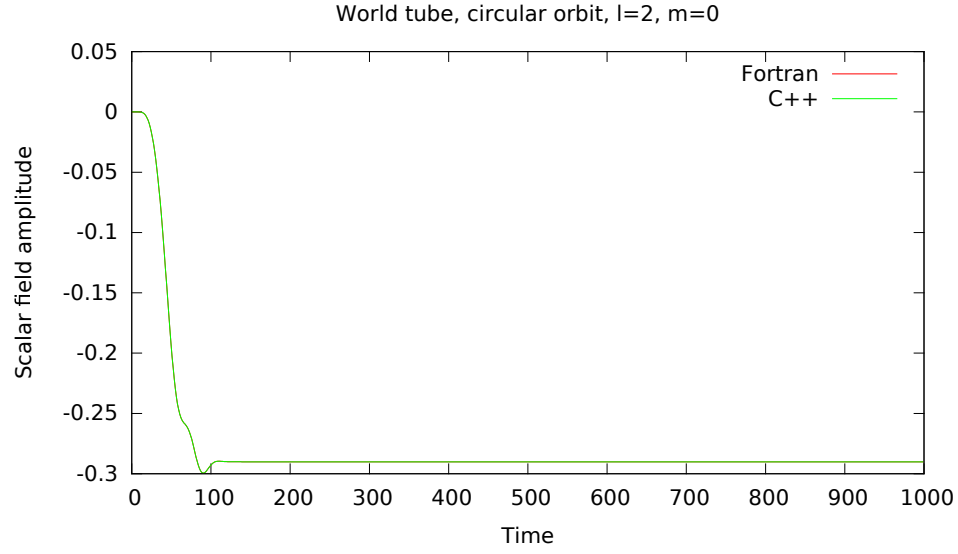


Figure 4.5: Comparison between Fortran and C++ codes for a particle on a circular orbit,  $l=2$ ,  $m=0$ .

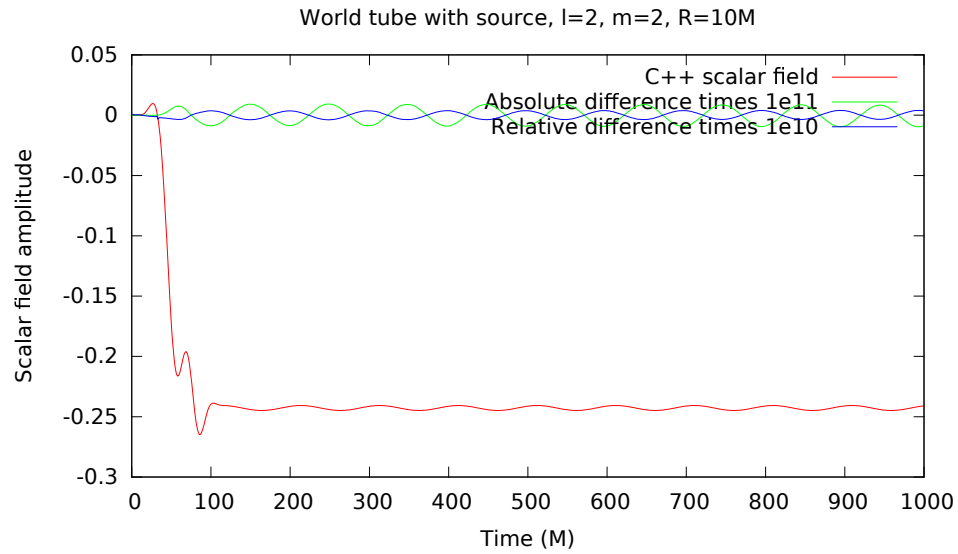


Figure 4.6: Comparison between Fortran and C++ codes for a particle on a circular orbit,  $l=2$ ,  $m=2$ .

# Chapter 5

## Elliptical orbits on a Schwarzschild spacetime

### 5.0.1 Time dependent coordinate transformation

wave equation

### 5.0.2 orbital parameters (osculating orbits paper)

### 5.0.3 precession figure

$\chi(t), \psi_r, \psi_{r\theta}, \psi_{r\phi}, \psi_{rt}$

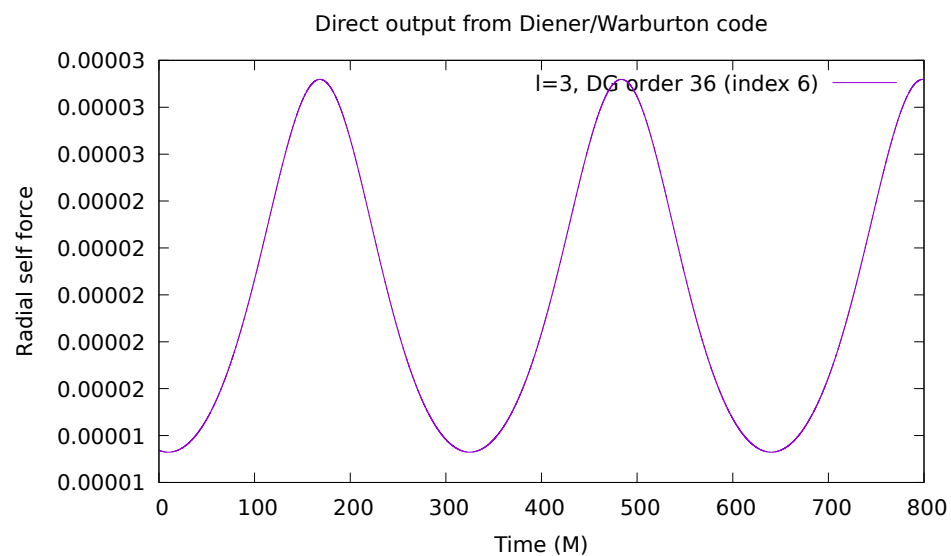
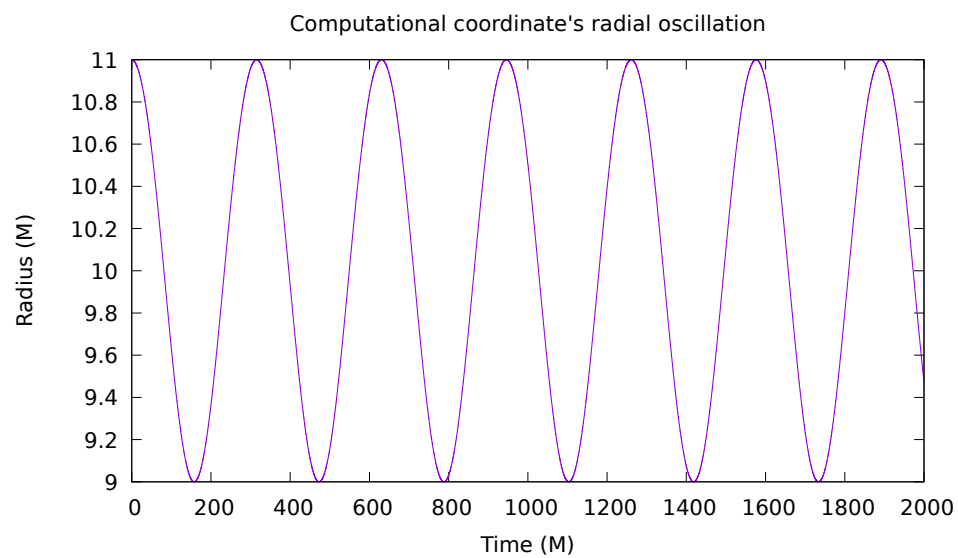


Figure 5.1: 470 M near perihelion, 640 M at aphelion

# Chapter 6

## Extrapolating the self force to infinite Discontinuous Galerkin order

Note that it is not always possible to choose three points such that they lie on a converging exponential form, for instance, if they are not monotonic, or if they curve in the wrong direction. In these cases, I say that the “mode failed”, and discard the result for that mode with that starting order for the extrapolation. I use extrapolation starting orders from the set 12, 16, 20, 24, 28, 32, and 36, with additional data at orders 40 and 44 that may be used as points two and three in the extrapolation.

### 6.0.1 Checking for discontinuities in $F_{\text{inf}}$ for each l-mode

In the median approach, the starting orders that did not “fail” at each time and for each mode are ordered by their  $F_{\text{inf}}$  values. The median value of  $F_{\text{inf}}$  is selected, presumably discarding those effected by roundoff and those effected by failure to converge. However, there is no guarantee that it selects those in this regime, since in principle a mode could both be in the roundoff limit and have not converged yet. Yet when this is done, there are no discontinuities in  $F_{\text{inf}}$  for any of the l-modes when the median approach is used. See mode zero for an example.

time	starting order	finf
632	0	mode failed
632	1	2.40975299617e-05
632	2	2.40975300465e-05
632	3	2.40975300114e-05
632	4	mode failed
632	5	2.40975299291e-05
632	6	2.40975299148e-05

Table 6.1: Manual starting indices and  $F_{\text{inf}}$  values for t=632, l=2.

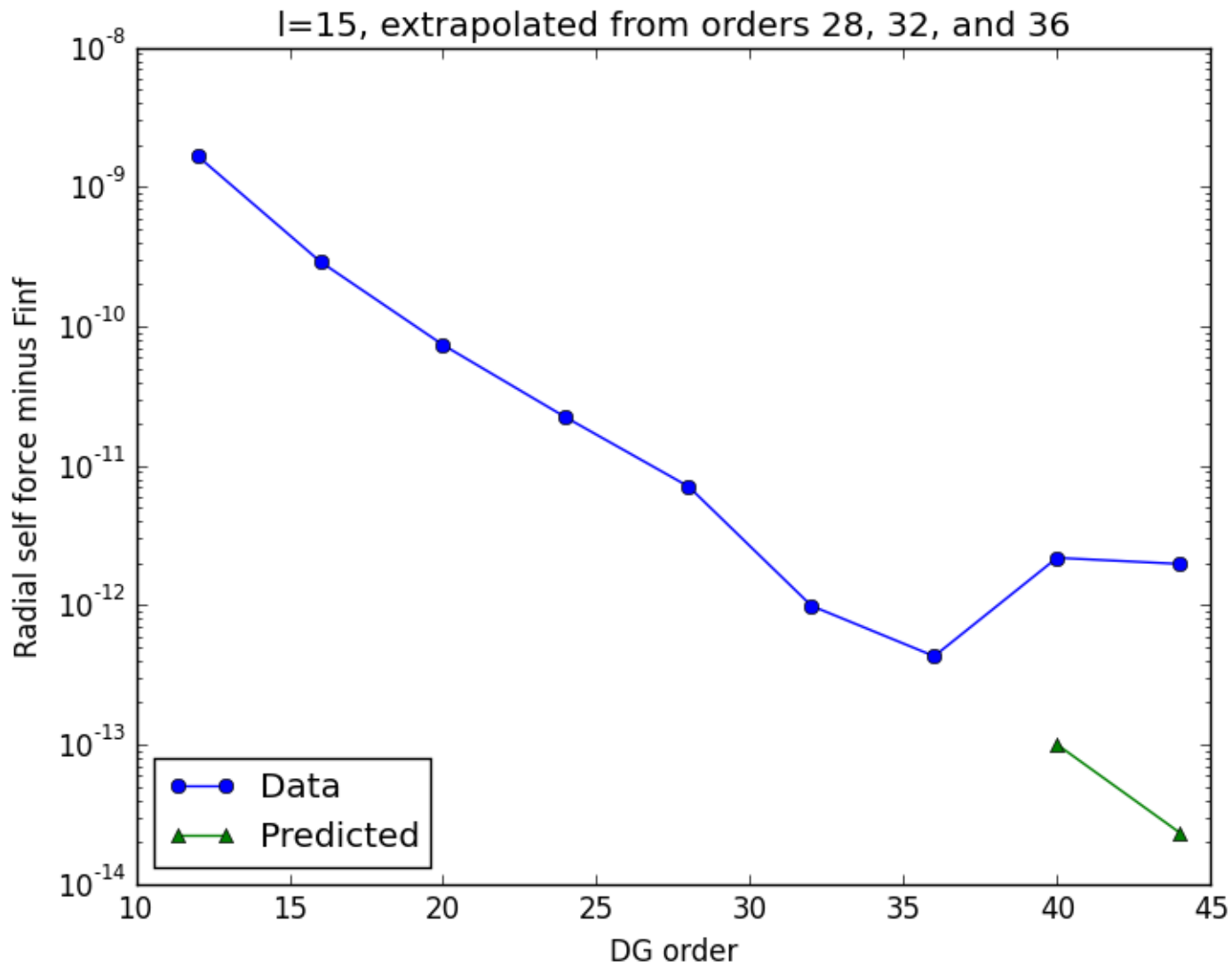


Figure 6.1: DG convergence with order, extrapolated from highlighted points to infinite order along exponential form, which appears as a straight line in the semilog plot.

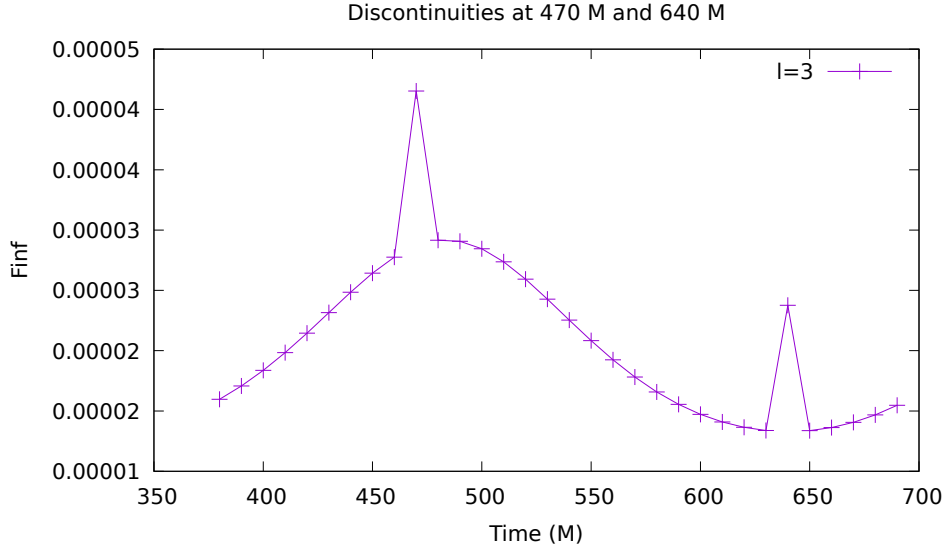


Figure 6.2: Starting order was chosen by iterating from the lowest order to the first order for which the “mode failed”, and choosing the maximum starting order that succeeded. When  $F_{\text{inf}}$  is evolved over one full orbital cycle, some l-modes show discontinuities at some times.  $l=3$

### 6.0.2 Determining $F_{\text{inf}}$ using maximum likelihood fits to subsegments of lines in semilog space

A better motivated approach, is to fit subsegments of lines in semilog space on the DG order convergence plot, and find the most linear, longest linear, region. A fit with the “best” value of the reduced chi squared should be a good approximation to this. The reduced chi squared is the value of the sum of the residuals of the fit squared divided by the number of degrees of freedom, which in this case is the number of points in the fit minus two, since there are two degrees of freedom in a linear fit. The expectation value of the reduced chi squared, in the limit of a large number of degrees of freedom, is one. I loop over starting and ending points of the fit, and over starting orders, and choose the starting order with the best fit line segment in the sense that that line segment has a reduced chi squared closest to one. An example of such an automatically chosen starting index is given in Figure ??, where there is a long exponentially converging region.

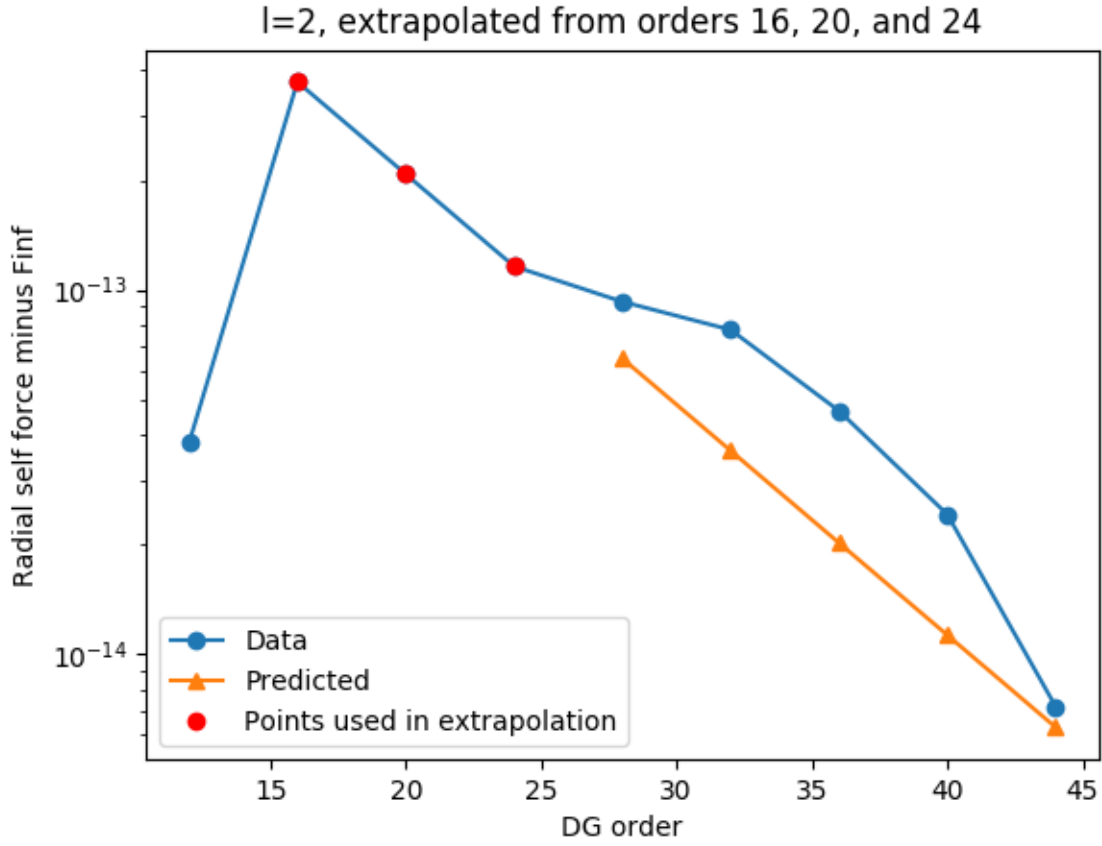


Figure 6.3: Fluctuation in one of the points chosen in the extrapolation, due to roundoff or truncation error, causes the extrapolation to predict a value of  $F_{\text{inf}}$  that is subtly wrong, leading to curvature in the semilog plot after  $F_{\text{inf}}$  subtraction.  $t=632$ ,  $l=2$ ,  $i=1$



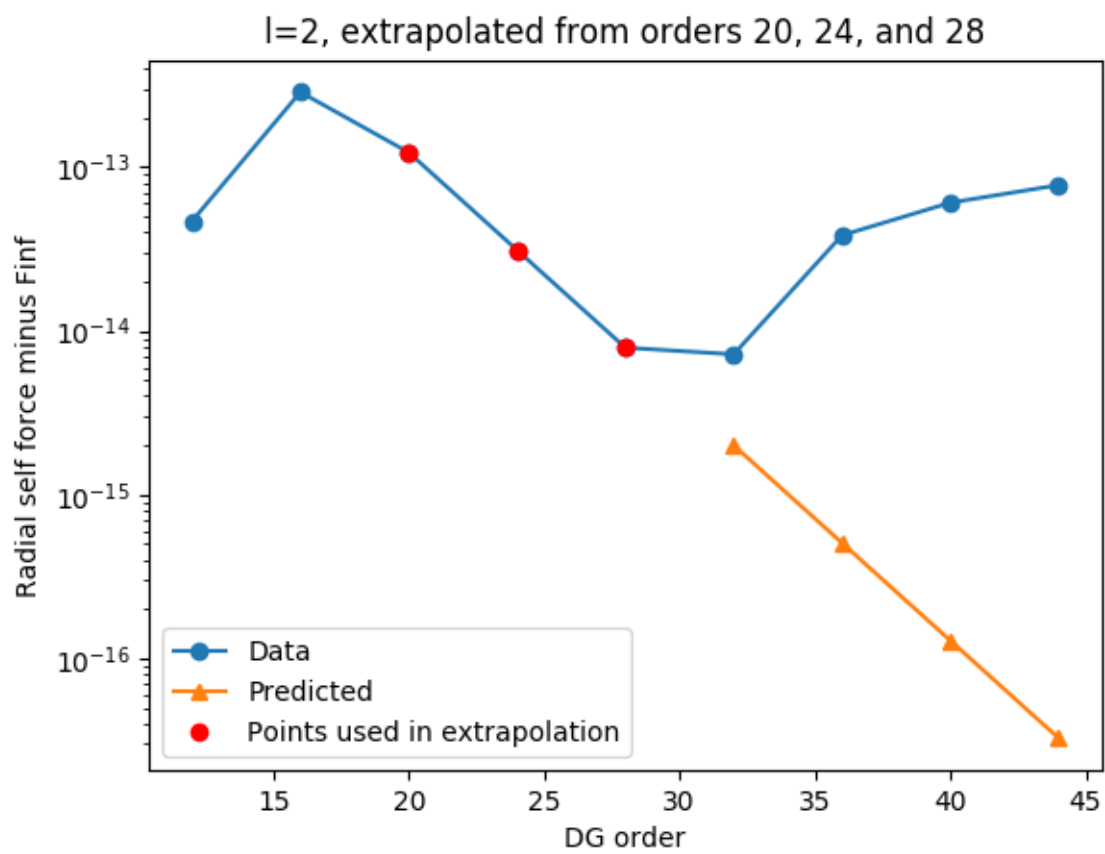


Figure 6.4: Roundoff error is visible at high DG orders.  $t=632$ ,  $l=2$ ,  $i=2$

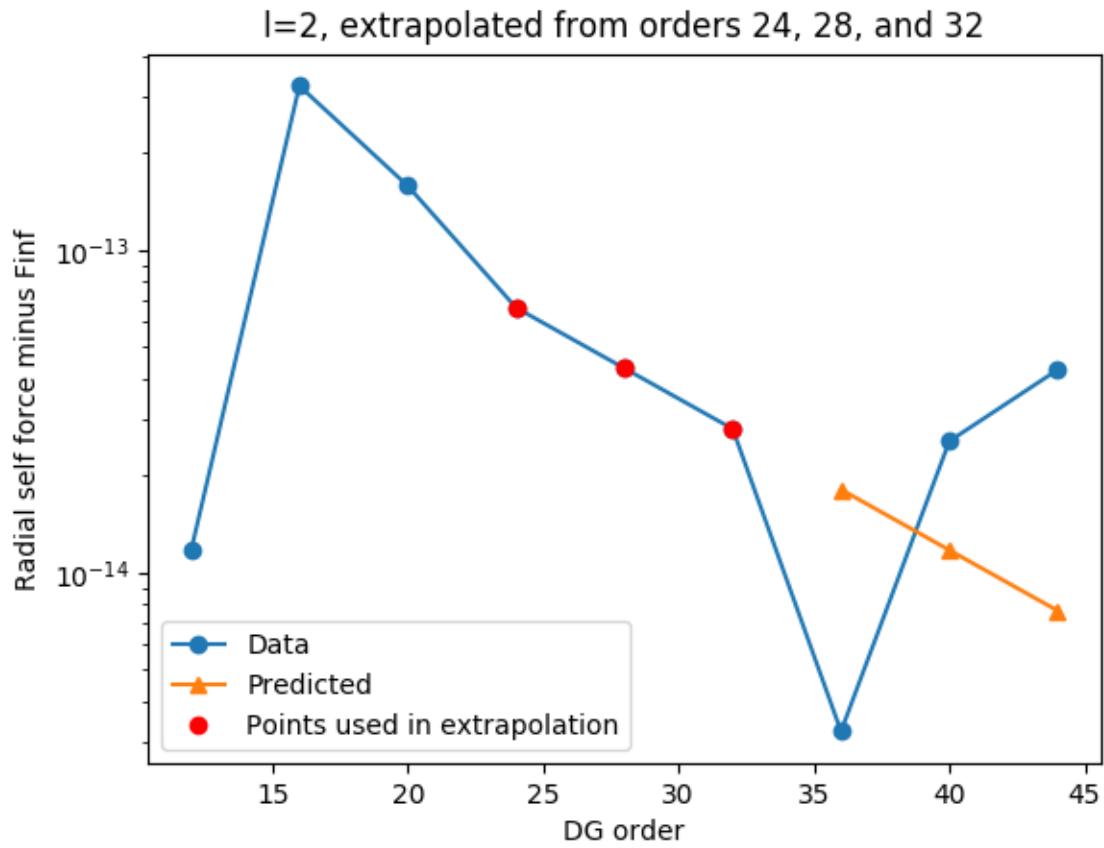


Figure 6.5: The incorrect value of  $F_{\text{inf}}$  has been chosen due to roundoff error, perhaps due to finite precision in the root finding algorithm, leading to a negative values, that show as a “V” in the semilog plot.  $t=632$ ,  $l=3$ ,  $i=3$

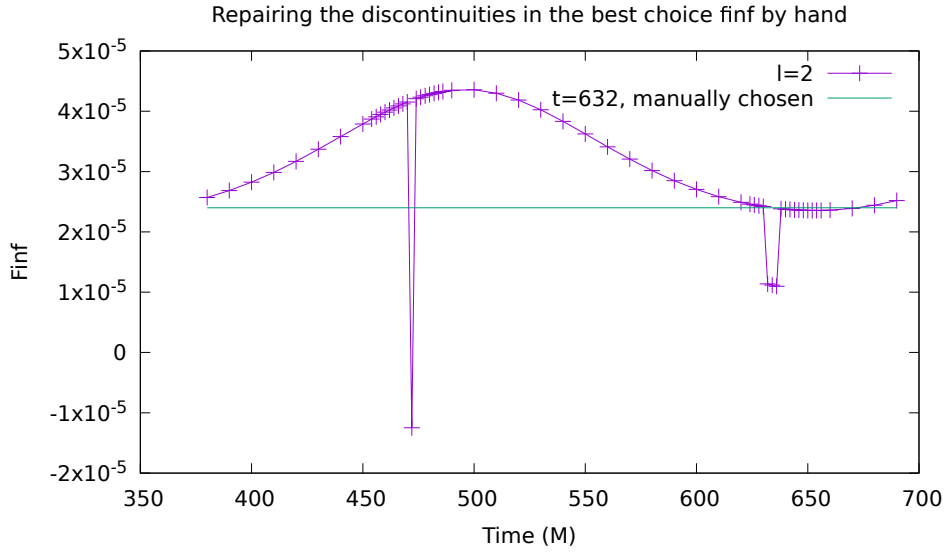


Figure 6.6: Manual correction for the discontinuities in the  $l=2$  mode, using the manually determined  $F_{\text{inf}}$  data from Table 6.1.



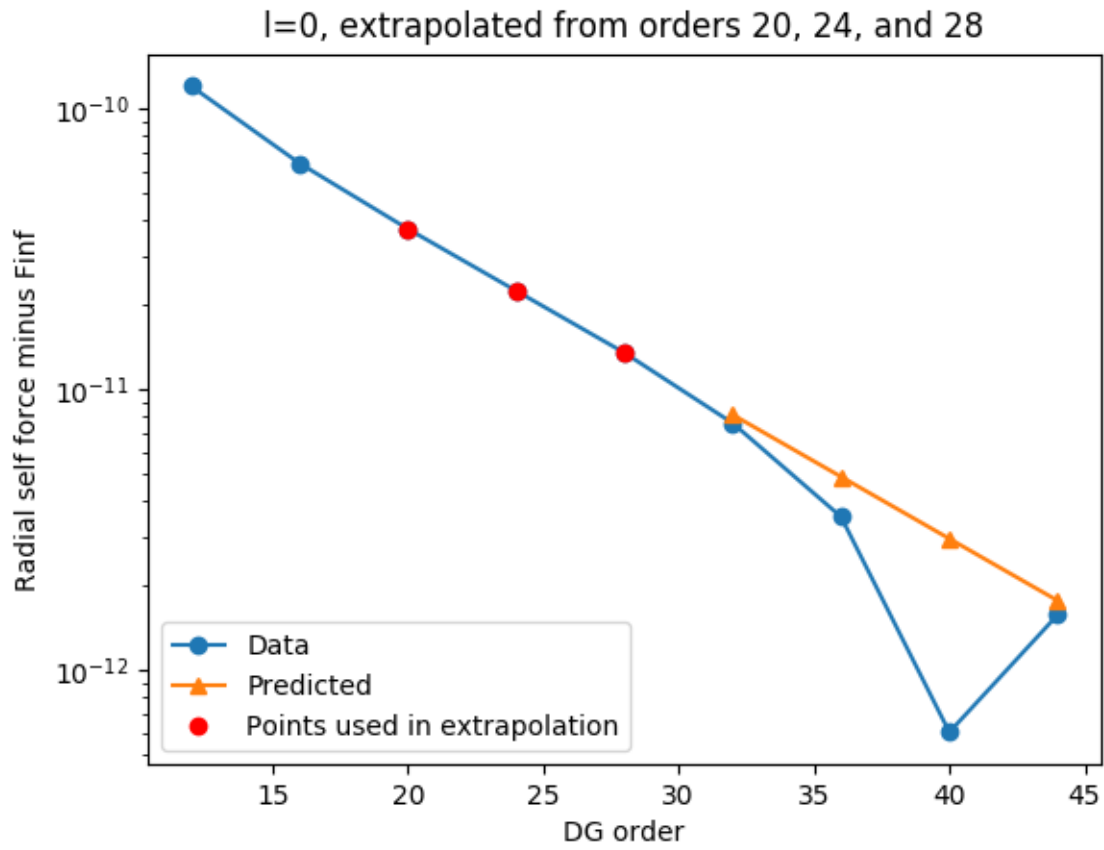


Figure 6.8:  $l=0$  mode with line-segment fit-chosen starting order produces convergence plot with long exponentially converging region

# Chapter 7

## Extrapolating the mode-summed self-force to include contributions from an infinite number of spherical harmonic modes

NEED A PLOT OF  $F_{\text{INF}}$  AS A FUNCTION OF  $L$

### 7.0.1 Relative error as a function of mode

We can understand why it is so hard to produce good fits by examining the relative error between different fitting techniques as a function of mode. Look at the relative error between the fit method and the median method. Both the relative and absolute error grow with  $l$ , explaining why the sigma-suppression technique does not produce good results.

NEED SOMETHING SHOWING FIT ITSELF. NEED TO REORDER AND RECAP-TION NEXT SECTION

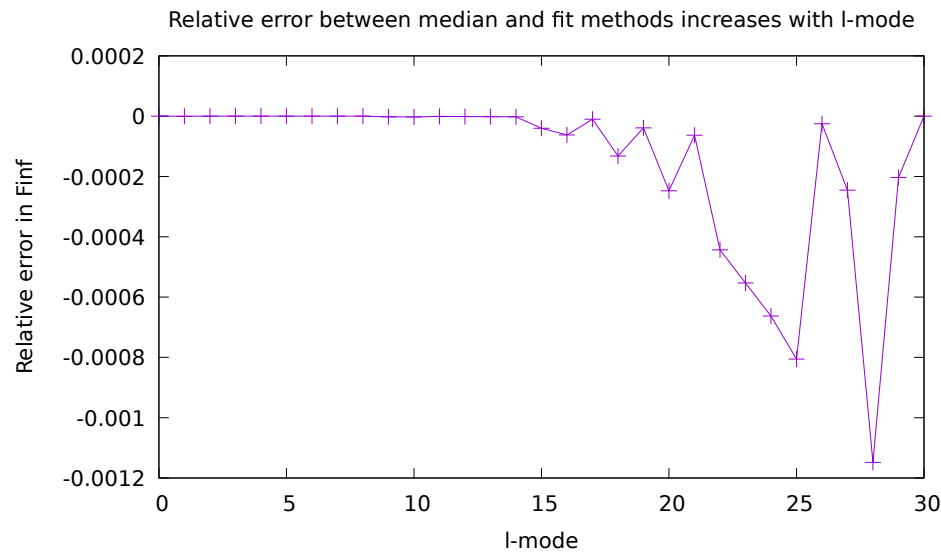


Figure 7.1: Relative error between fit and median techniques increases with l-mode

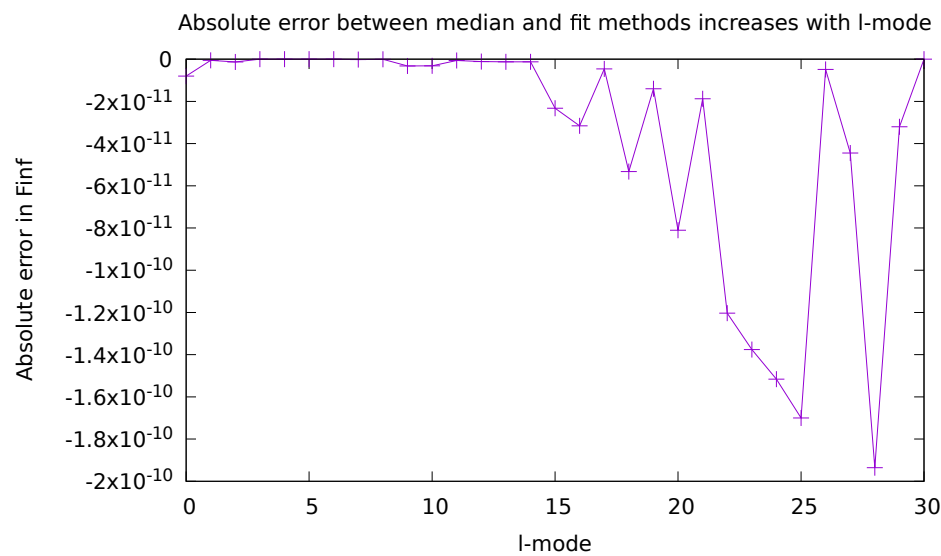


Figure 7.2: Absolute error between fit and median techniques increases with l-mode

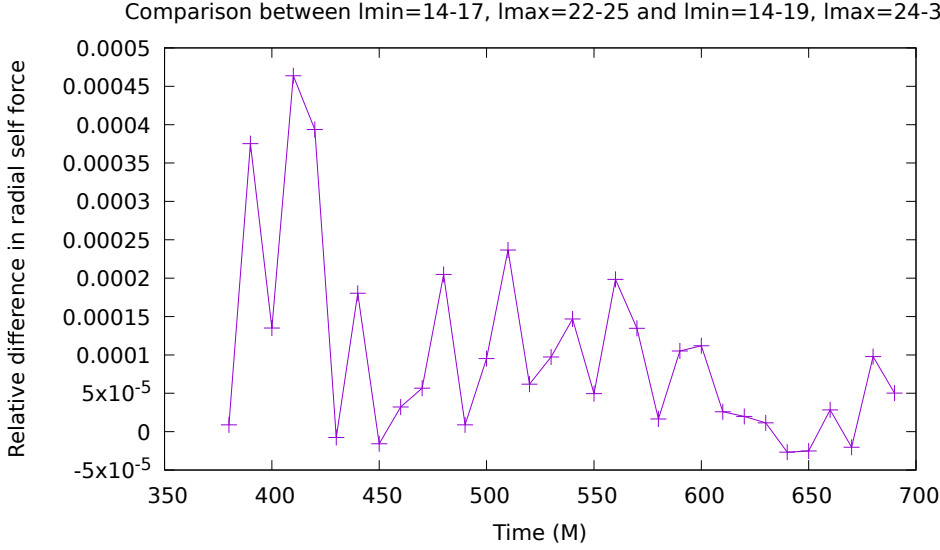


Figure 7.3: This is the relative difference between the total radial self force measured in two different ways. In both cases, the self force was extrapolated to infinite order at every  $l$ -mode at every possible DG starting order. The infinite DG order self forces over the various starting orders were sorted, eliminating NaNs. The median was chosen for each  $l$ -mode. Then the self force as a function of  $l$ -mode was fit to its three term form, and the sum was summed from zero to  $l_{\max}$ , then extrapolated from  $l_{\max} + 1$  to infinity using an analytic form determined using Mathematica. All possible choices with  $l_{\min}$  between 14 and 17 and  $l_{\max}$  between 22 and 25 were averaged to obtain the total radial self force as a function of time. Similarly, all possible choices with  $l_{\min}$  between 14 and 19 and  $l_{\max}$  between 24 and 30 were averaged to obtain the total radial self force as a function of time. This plot shows the relative difference. I believe the smaller range is in the denominator.



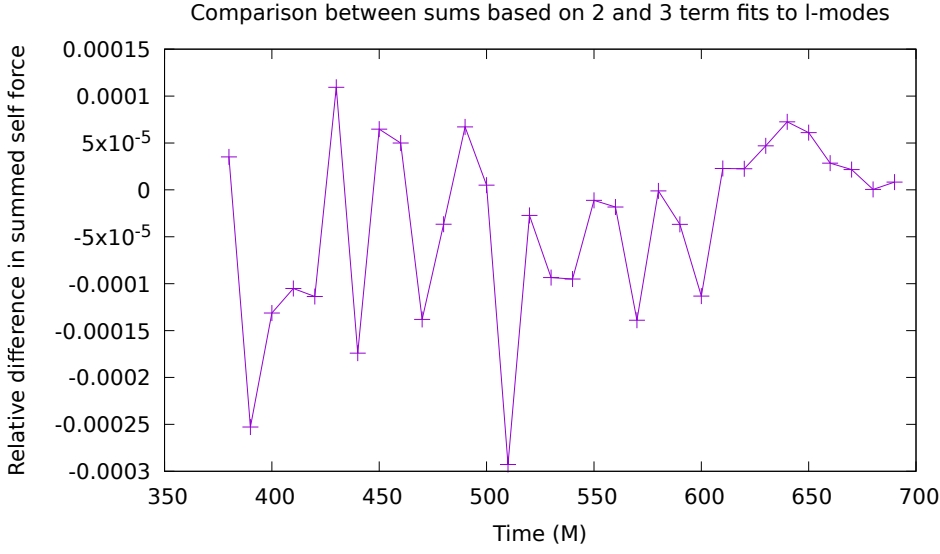


Figure 7.4: This figure was produced in the same manner as the previous figure, averaging over the smaller range, only it is a comparison between including either two or three terms in the l-mode fit. I believe the three term fit is in the denominator of the relative difference.

take standard deviation of surface plot as well as average.

## 7.0.2 Fractional errors

## 7.0.3 Structure of the error compared to the evolution in time

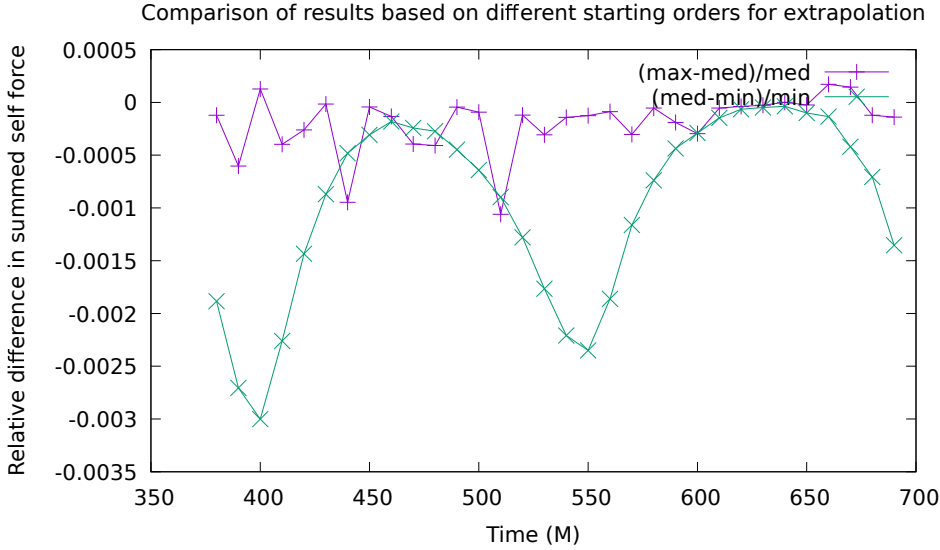


Figure 7.5: This figure was produced in a similar manner to the first figure, only instead of using the median, it is a comparison between using the median, the maximum, and the minimum. The purple line is the relative difference between the maximum and the median, which is subject to roundoff error due to the potential for the maximum to contain roundoff error. The green line is the relative difference between the median and the minimum, which is subject to effects due to failure to converge. I suspect the median is the best compromise between these two effects, rejecting outliers in both directions, though it is a simplistic approach to doing so, and does not guarantee success. It is possible to have a starting order that has not converged and is also in the roundoff regime, for example. A better guarantee of success, though not a certain one, would be to do a fit over part of the error convergence plot to determine exponentiality, by fitting a line in semilog scale. However, this seems unnecessarily complex at this time.

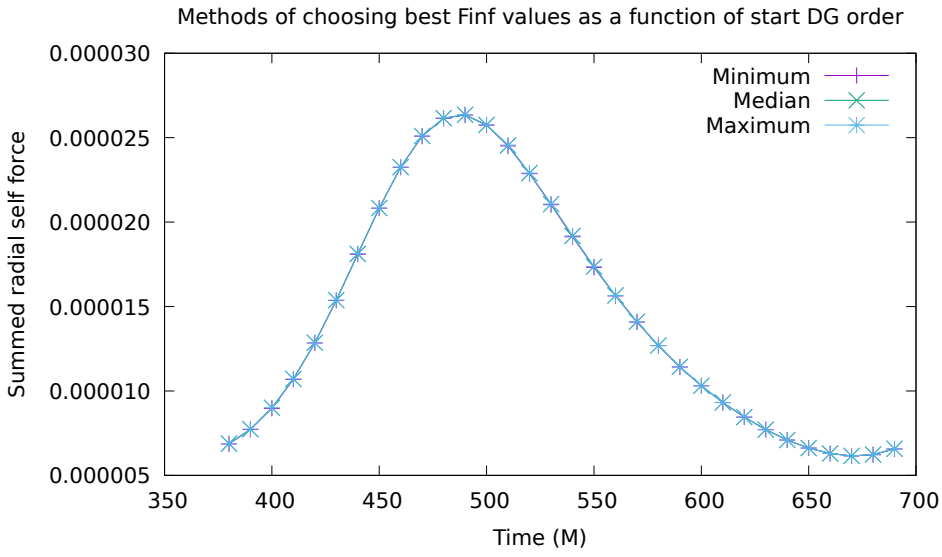


Figure 7.6: This is the actual summed, doubly extrapolated, radial self force, measured in three different ways as described in the three figures above.

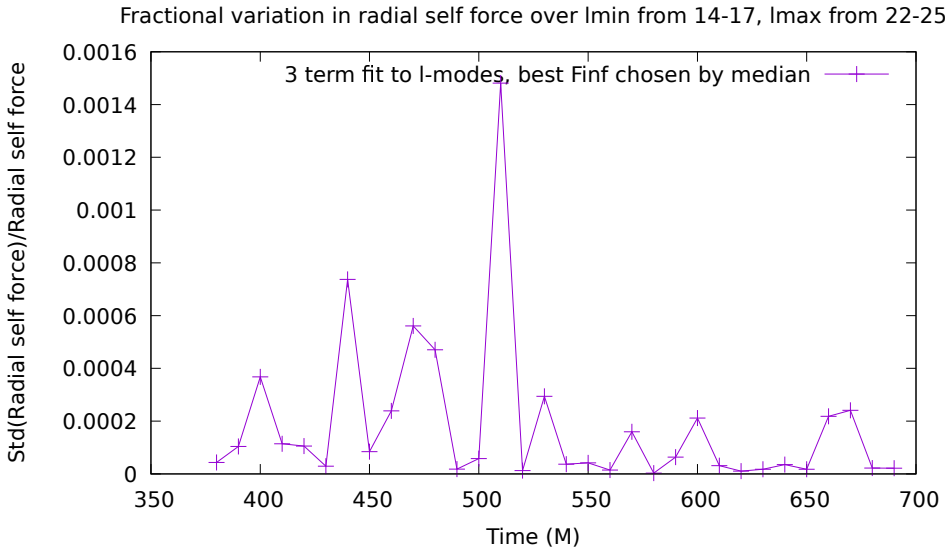


Figure 7.7: 3 term, median method

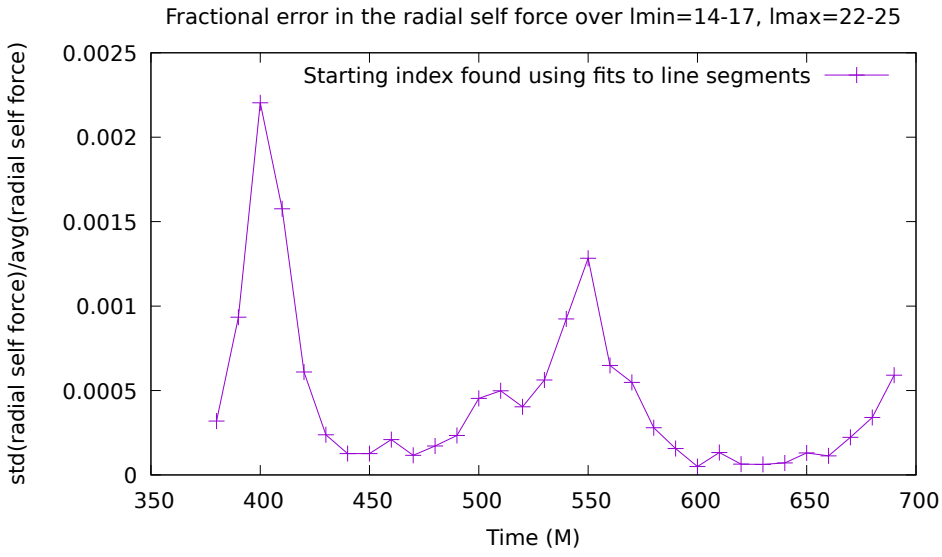


Figure 7.8: 3 term, fit method

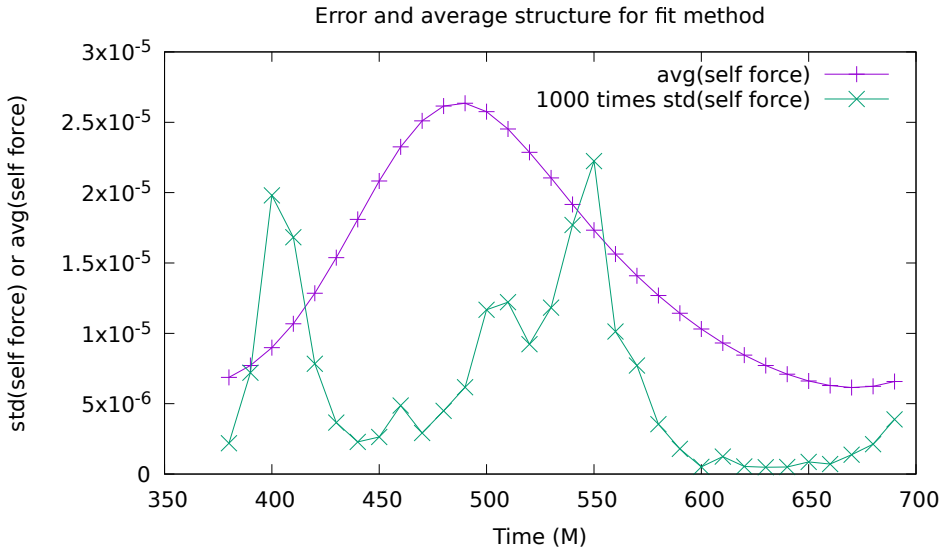


Figure 7.9: The structure of the absolute error in comparison to the evolution in time for the fit method

# Chapter 8

## Future work: generic orbits via the osculating orbits framework

### 8.1 plans for the future

going to test Peter Diener's generic orbits and help him develop them further.

#### 8.1.1 methods

effective source osculating orbits time dependent coordinate transformation world tube already implemented with accelerated orbits though I have not run these. future work: make self consistent evolution work.

# References

- [1] LIGO Virgo Collaboration. (2016). Observation of Gravitational Waves from a Binary Black Hole Merger. *Phys. Rev. Lett.* 116, 061102.
- [2] LIGO Virgo Collaboration. (2016). GW151226: Observation of Gravitational Waves from a 22-Solar-Mass Binary Black Hole Coalescence. *Phys. Rev. Lett.* 116, 241103.
- [3] LIGO Virgo Collaboration. (2017). GW120104: Observation of a 50-Solar-Mass Binary Black Hole Coalescence at Redshift 0.2. *Phys. Rev. Lett.* 118, 221101.
- [4] LIGO Virgo Collaboration. (2016). Observing Gravitational-wave Transient GW150914 with Minimal Assumptions. *Phys. Rev. D* 93, 122004.
- [5] LIGO Virgo Collaboration. (2016). GW150914: First Results from the Search for Binary Black Hole Coalescence with Advanced LIGO. *Phys. Rev. D* 93, 122003.
- [6] LIGO Virgo Collaboration. (2016). The Rate of Binary Black Hole Mergers Inferred from Advanced LIGO Observations Surrounding GW150914. *Accepted Astrophys. J. Lett*
- [7] LIGO Virgo Collaboration. (2016). Astrophysical Implications of the Binary Black-Hole Merger GW150914. *Astrophys. J. Lett* 818, L22.
- [8] LIGO Virgo Collaboration. (2016). Tests of General Relativity with GW150914. *Phys. Rev. Lett.* 116, 221101.
- [9] LIGO Virgo Collaboration. (2016). GW150914: Implications for the Stochastic Gravitational Wave Background from Binary Black Holes. *Phys. Rev. Lett.* 116, 131102.
- [10] LIGO Virgo Collaboration. (2016). Calibration of the Advanced LIGO Detectors for the Discovery of the Binary Black-hole Merger GW150914. *Submitted to Phys. Rev. D*.
- [11] LIGO Virgo Collaboration. (2016). Characterization of Transient Noise in Advanced LIGO Relevant to Gravitational Wave Signal GW150914. *Class. Quant. Grav.* 33, 134001.
- [12] LIGO Virgo Collaboration and ANTARES and IceCube Collaborations. (2016). High-energy Neutrino Follow-up Search of Gravitational Wave Event GW150914 with ANTARES and IceCube. *Phys. Rev. D* 93 122010.
- [13] LIGO Virgo Collaboration. (2016). GW150914: The Advanced LIGO Detectors in the Era of First Discoveries. *Phys. Rev. Lett.* 116, 131103.
- [14] LIGO Virgo, ASKAP, BOOTES, Dark Energy Survey and Camera, GW-EM, Fermi GBM and LAT, GRAWITA, INTEGRAL, IPTF, InterPlanetary, J-GEM, La Silla-Quest, Liverpool Telescope, LOFAR, MASTER, MAXI, MWA, PAN-STARRS, PESSTO, PI of the Sky, SkyMapper, Swift, TAROT, Zadko, Algerian National

- Observatory, C2PU, TOROS, and VISTA Collaborations. (2016). Localization and Broadband Follow-up of the Gravitational-wave Transient GW150914. *Astrophys. J. Lett.* 826, L13.
- [15] Bambi, Cosimo. (2017) Testing black hole candidates with electromagnetic radiation. *Reviews of Modern Physics* 89.
  - [16] Martynov, D.V., et al. (2016). Sensitivity of the Advanced LIGO detectors at the beginning of gravitational wave astronomy. *Phys. Rev. D* 93, 112004.
  - [17] Poisson, Eric; Pound, Adam; Vega, Ian. (2011). The motion of point particles in curved spacetime. *Living Reviews in Relativity.* 14, 7.

# Vita

My past research has been on comet photometry, x-ray bursts, gravitational lensing and cosmology, exoplanets, neutrino oscillations, theoretical particle physics, gravitational waves, and gravity gradient noise. Most of my background is in simulation, whether statistical or theoretical. I think of myself as a computational physicist and a multimessenger astronomer, though I am not sure that term is widely used. What I mean by it is that I have a broad background in particle physics, particle astrophysics, gravitational wave astronomy, and traditional astronomy. If we can consider my various meanderings as one path toward these two goals, I have been walking this path for more than a decade.

Now I am a fourth year graduate student at Louisiana State University, exactly where I intended to be. My coworkers are good friends. I got to perform photometry of exoplanets with a telescope and analyze the data for myself, bringing a previous project full circle. I have worked on LIGO during the time of three detections. I have had the opportunity to begin to learn multiple techniques for speeding up code and measuring that speed up on supercomputers. I have done a little work with databases and more with numerical algorithms, and learned a couple of new programming languages. I have had the opportunity to continue to contribute to the field of general relativity and participate in a department where my broad background in the connections between various fields of astronomy is valued. I have helped supervise undergraduate research progress and made a lesson plan for and taught a graduate class, once. This document contains the research I have produced in the last three years since I arrived on June 3, 2014 at LSU and began working with Peter Diener. These have been the best three years of my life.

When interpreting the name on this document, please understand that I am female to male transgendered and that my legal name is Susan Elaine Dorsher but that I go by Steven James Dorsher.